Supporting material: Enhanced deposition of sickle cells at acute corners and its possible role in vaso-occlusion

Etienne Loiseau
Université Montpellier 2 and CNRS UMR 5221,
Laboratoire Charles Coulomb, Montpellier, F-34095, France

Gladys Massiera
Université Montpellier 2 and CNRS UMR 5221,
Laboratoire Charles Coulomb, Montpellier, F-34095, France

Simon Mendez
Université Montpellier 2 and CNRS UMR 5149,
Institut de Mathématiques et de Modélisation de Montpellier,
Montpellier, F-34095, France

Patricia Aguilar Martinez
Hôpital Saint Eloi,
Laboratoire d'Hématologie, Montpellier, France

Manouk Abkarian[1]
Université Montpellier 2 and CNRS UMR 5221,
Laboratoire Charles Coulomb, Montpellier, F-34095, France

[1]Corresponding author: Manouk.Abkarian@univ-montp2.fr. Address: Université Montpellier 2 and CNRS UMR 5221, Laboratoire Charles Coulomb, Montpellier, F-34095, France, Tel.: 33 (0)4 67 14 39 82, Fax: 33 (0)4 67 14 46 37

1 Method

1.1 Soft lithography

Devices are fabricated using the classical soft-lithography with replica molding method (1). They are made of a silicone elastomer, the polydimethylsiloxane (PDMS) which allows gas exchange (2). The desired design is created with a computer-aided design software (Clewin, WieWeb Software, Netherlands), which we print on a transparency (for ÃŠlargeÃŞ features between 10 and 200 μm) by a high-resolution commercial image setter. This transparency serves as the photomask in contact photolithography. The soft lithography step produces a positive relief of photoresist (SU-8, MicroChem Corp, USA) on a silicon wafer. The speed of the spin-coater sets the thickness of this layer of photoresist, controlling the height of the channels. Then, we pre-bake the wafer for several minutes at 65°C and 95°C (exact times depends on the brand of the photoresist and the desired thickness) in order to initiate the polymerization of the SU-8. A UV source is used to expose the silicon wafer covered with the photomask. Another baking step finishes to cure the photoresist. Dissolving away the non-illuminated — and so the non-polymerized — photoresist leaves a positive relief that serves as a master. Then PDMS channels are formed by replica molding (ridges on the master appear as valleys in the replica). We mix the solution of silicone elastomer with a curating agent (Sylgard 184 kit silicone elastomer, Dow Corning) in a ratio 10/1 and homogenize the mixture. After pouring the solution into a petri dish over the master, we degas under a vacuum in order to get rid of any bubbles. The whole preparation is cured in an oven at 65°C for 1 hour. The replica is then peeled from the master and access holes are punched out of the cured layer by using a truncated needle before assembly.

Since PDMS is porous to gas, we use this feature to control the oxygen concentration in the channels via a two-layer device. The first layer of 60 μm in thickness is engraved with channels of 30 μm high where RBCs flow. This layer is bonded to a glass microslide using a corona discharge for tens of seconds produced by a hand-held discharge unit (Electro-Technic Products, model BD-20AC) with an output voltage of 25 kV. If a rubber-like polymer such as PDMS is placed under such a corona discharge, the charged particles that are generated deposit on the surface, where they initiate radical reactions that modify the rubber surface by creating functional groups (e.g. Si-OH), which are used to bond covalently PDMS to PDMS or to glass. The treatment has to be fast because the PDMS gas permeability decreases while exposed to the corona discharge (3). The second layer, dedicated to the gas flow is bonded on the top of the first one. The channels are 500 μm width and 80 μm high and cover all of the surface of the chip to maximize the gas exchange.

2 Description of the numerical simulations

Two types of computer simulations are performed to support the analysis of the experimental results. First, the flow around a triangular pillar is computed, in the absence of cells. Then, two-dimensional simulations illustrate how deformable objects may interact when flowing around a pillar. All the simulations were performed using YALES2BIO (http://www.math.univ-montp2.fr/-

∼yales2bio), an in-house flow solver developed at the I3M. It is based on the YALES2 solver (http://www.coria-cfd.fr/index.php/YALES2), developed at CORIA, in Rouen (France). YALES2BIO is dedicated to the simulations of blood flows, either with or without the presence of deformable cells (4–6).

2.1 Numerical simulations of the flow around a pillar

The complete geometry of the RBC channel (displayed in figure 1 of the paper) is complex. The ratio between the smallest geometrical length scales and the length of the channel is also very small. A full computation of the flow in the channel would thus be tedious. The objective here is to get information about the flow around one triangular pillar. However, pillars are surrounded by other pillars, which makes the computation of the flow around one isolated pillar irrelevant. It was thus decided to compute an asymptotic case, in which the fluid flows around an infinite number of pillars, arranged in a staggered manner, as in the experiment. In this configuration, it is possible to reduce the computational domain using periodic boundary conditions. Such a technique is classical for computations for channel flows (7) and has also been used for more complex flows (8).

2.1.1 Geometry

The geometry of the computational domain is shown in figure S4. The periodic array of pillars is suggested in the figure by the presence of the neighboring pillars, drawn in dashed lines. Three pairs of periodic boundary conditions delimitate the frontiers of the computational domain (thin solid lines). In the z direction, the computational domain has a height of $h = 30$ μm: it is closed by impermeable walls at $z = \pm 15$ μm. Pillars are staggered in space, the distance between two pillars being $L = 200$ μm. The pillar itself is an isosceles triangle with rounded corners. We denote by c1 the left corner (leading edge) and c2 and c3 the right (downstream) corners. The radius of curvature for the corners is 4 μm for c1 and 5 μm for c2 and c3. The 'heights' of the pillar are 54 μm from c1 to the opposite edge and 50 μm from c2 (resp. c3) to the opposite edge (the angle of c1 is approximately 54 degrees).

2.1.2 Boundary Conditions

Periodic boundary conditions are applied on the three pairs of frontiers of the hexagonal domain (thin solid lines in figure S4). In order to generate the flow, a mean pressure gradient is imposed via a constant source term in the x direction. Non-slipping wall boundary conditions are applied on the pillar surface. In the z direction, non-slipping wall boundary conditions are applied at $z = \pm 15$ μm.

2.1.3 Grid

In order to compute the flow in this periodic domain, it is discretized using tetrahedral cells. The tetrahedral grid used is composed by 2.35 million elements. The grid resolution is set to 2 μm far

from the pillar (near the periodic boundary conditions) and smoothly decreases to reach 1 μm near the pillar. No significant change in the results has been observed by refining the grid.

2.1.4 Model and numerics

In this discretized domain, the incompressible Navier-Stokes equations are solved:

$$\boldsymbol{\nabla}.\vec{u} = 0, \tag{1}$$

$$\rho\,(\frac{\partial \vec{u}}{\partial t} + \vec{u}.\boldsymbol{\nabla}\vec{u}) = -\boldsymbol{\nabla}p + \boldsymbol{\nabla}.[\mu(\boldsymbol{\nabla}\vec{u} + (\boldsymbol{\nabla}\vec{u})^T)] \; + \; S\,\vec{e_x}, \tag{2}$$

where ρ and μ are the constant density and the dynamic viscosity of the fluid, respectively. $\vec{u}$ is the fluid velocity, p the pressure and t the time. The flow is maintained from left to right thanks to an additional source term S in the momentum equation in the x direction. The forced unsteady Navier-Stokes equations are solved using a fourth-order finite-volume scheme. YALES2BIO solves the unsteady Navier-Stokes equations using a projection method. A fourth-order Runge-Kutta scheme is used to advance the velocity field and the Deflated Preconditioned Conjugate Gradient method (6, 9, 10) is used to solve the Poisson equation for pressure.

2.1.5 Operating point

The kinematic viscosity is set to $\nu = \mu/\rho = 1.2 \times 10^{-6}$ m^2.s^{-1}. The source term is adjusted in order to obtain a mean velocity of the order of the ones encountered in the experiment. The bulk velocity is 110 μm.s^{-1}. The resulting flow is in the creeping flow regime: the Reynolds number based on the channel height of h and the bulk velocity is approximately 0.0028. The computation is run for several characteristic times h^2/ν to obtain time-converged results. In order to guarantee the accuracy of the solution, results were double checked by verifying that they match results obtained using a commercial software and a creeping flow hypothesis. In addition, we verified that the three-dimensional flow structure corresponds well to existing data on creeping flows around corners (11).

2.2 Numerical simulations of capsules flowing around the pillar

In order to illustrate how flowing cells may interact while passing around the pillar, 2-D numerical simulations of the dynamics of capsules are performed. Two-dimensional configurations were considered to shorten the calculation times. Some simulation parameters differ from the experimental values. These choices were made to obtain reasonable computational times while keeping the essential ingredients present in the experiment. The 2-D simulations are not an attempt to mimic the experiment. They are to be considered as an illustration of how particles flowing around the pillar corner may interact to explore otherwise forbidden regions of the flow. Numerical simulations of the experiment should include accurate membrane mechanics and membrane viscosity for 3-D

red blood cells, with potential adhesion effects, in a dense suspension and with complex geometry in a large channel and for long characteristic times. Such simulations are out of reach of current softwares, but we hope that the simple computations presented here will motivate groups to study the flows of red blood cells around complex geometries using numerical simulations.

2.2.1 Geometry

The configuration of interest is the flow of inextensible capsules around a pillar, in 2-D. In that case, the geometry and the boundary conditions correspond to the 3-D case described earlier, except that the domain is now infinite in the z direction. The configuration is shown in figure S5(a).

Either one isolated capsule or two capsules, one behind another (as shown in figure S4), are deposited in the flow. The capsules are initially elliptic with the large radius of 4 μm and a small radius of 1 μm (the surface ratio). The corresponding equivalent radius (radius of the circle of same area) is $R = 2.7$ μm. The reduced area (ratio of the capsule area over the area of circle of the same perimeter) is 0.54. In the case with two capsules displayed, the initial distance is between the capsules is 0.5 μm. Capsules are deposited with an initial distance to the wall of 0.75 μm, just upstream of the corner. When capsules are positioned further upstream from the corner, the wall-associated lift has time to act and capsules pass the corner far from the wall.

2.2.2 Boundary conditions

The boundary conditions correspond to what is done in the 3D simulations in the absence of capsule, except in the z direction, which is now infinite. Non-slipping wall boundary conditions are applied at the surface of the pillar. The numerical domaine is delimited by three pairs of periodic boundary conditions (thin solid lines in figure S5a). As in 3D, as there are no inlets/outlets in this configuration, the flow is maintained by imposing a constant source term, as in the previous three-dimensional simulation.

2.2.3 Grid

Computational domains are discretized using unstructured triangular grids. They are refined in the region where the capsules flow, where the grid resolution is of order of 0.3 μm. The membrane is discretized with 64 markers. The order of magnitude of the grid sizes corresponds to what is used in the numerical simulations used to validate the software in the paper by Mendez *et al.* (4).

2.2.4 Model

A fluid-structure interaction method dedicated to the computation of the dynamics of capsules and vesicles under flow is implemented in the YALES2BIO flow solver (4). The Navier-Stokes flow solver described earlier is modified to account for the presence of deformable objects. The method is based on the immersed boundary technique (12, 13) for infinitely thin membranes, initially developed for Cartesian fluid grids and adapted to unstructured finite-volume formulations (4). This method

is a one-fluid method in which forced Navier-Stokes equations are solved everywhere, on a fixed Eulerian grid:

$$\boldsymbol{\nabla}.\vec{u} = 0, \tag{3}$$

$$\rho\,(\frac{\partial \vec{u}}{\partial t} + \vec{u}.\boldsymbol{\nabla}\vec{u}) = -\boldsymbol{\nabla}p + \boldsymbol{\nabla}.[\mu(\boldsymbol{\nabla}\vec{u} + (\boldsymbol{\nabla}\vec{u})^T)] \;+\; S\,\vec{e_x} \;+\; \vec{f}. \tag{4}$$

In order to account for the presence of the particles, a source term $\vec{f}$ modeling the forces exerted by the membrane on the fluid is added in the momentum conservation equation (Eq. 4). This force is calculated on the membrane markers, which are tracked in a Lagrangian way, and then regularized on the Eulerian fluid grid (see Mendez *et al.* (4) for numerical details). This force has an elastic component and a bending component (14) ($\vec{f} = \vec{F}^{leas} + \vec{F}^{bend}$) and is applied only in the vicinity of the membrane. The elastic component is obtained by assuming that two neighboring markers of the membrane are linked by a Hookean spring of elastic modulus E_e. The bending component of the force is calculated from the functional derivative of the Helfrich energy (15):

$$\mathcal{E}_b \;=\; \frac{E_b}{2}\int_S \kappa^2\,dS, \tag{5}$$

where E_b is the membrane bending modulus, κ the curvature (inverse of the radius of curvature; with $\vec{n}$ the outward pointing normal vector to the membrane, $\kappa = \boldsymbol{\nabla}.\vec{n}$). Spontaneous curvature is supposed to be zero. The associated force exerted by the membrane on the fluid reads

$$\vec{F}^{bend} \;=\; E_b\,[\frac{1}{2}\,\kappa^3 \;+\; \Delta_{LB}\,\kappa]\,\vec{n}, \tag{6}$$

where Δ_{LB} is the Laplace-Beltrami operator, *ie*: $\Delta_{LB} = (\mathbf{I}_s\boldsymbol{\nabla}).(\mathbf{I}_s\boldsymbol{\nabla})$ and $\mathbf{I}_s = \mathbf{I} - \vec{n}\vec{n}$ (16).

The capsules deposited are actually almost inextensible and resist bending. Such an object is often referred to as vesicle (14). In 2-D, the difference is minimal. Such 2-D objects are often used in the literature to demonstrate physical phenomena (14, 17–20) relevant to elastic capsules, lipid vesicles or red blood cells. Extensive validation of the solver is presented by Mendez *et al.* (4)

2.2.5 Operating point

In order to accelerate the computation, a bulk velocity of 18 mm.s^{-1} is imposed. In the region where the particles are deposited, the shear k is such that the particle Reynolds number is $k\,R^2/\nu \approx 5 \times 10^{-3}$, which is small and guarantees the absence of inertial lift at the scale the capsules. The capillary number, based on the elastic coefficient of the membrane E_e is $Ca = \mu\,k\,R/E_e = 0.002$, which ensures that the membrane perimeter varies of less than 0.5% during the calculations. The bending coefficient E_b is such that $E_b/(E_e\,R^2) = 0.001$. The viscosity is identical inside and outside the capsule.

2.2.6 Control numerical experiment

A second test case with capsules is used as a control numerical experiment: it is a simple 2-D Couette flow between two flat walls. The configuration is shown in figure S5(b). The Couette domain is a rectangle of length 500 μm and height 100 μm. This domain is used to compare the dynamics of capsules around a corner and along a flat wall. The model, grid resolution and the characteristic parameters (shear rate, capillary number, Reynolds number, bending coefficient) are strictly identical to the case of flowing capsules around a pillar, described in the former subsections. In this Couette flow, the shear rate is constant and identical to the one seen by the capsules when they flow along the lateral wall of the pillar.

Couette flow simulations were used as control cases, to confirm that the specific results obtained around the pillar are related only to the flow geometry. In the Couette flow, capsules simply interact by switching positions, as observed in computations of two interacting vesicles or capsules (21) in the presence of a wall. The specific phenomenon shown in the paper of capsules exploring regions very close to the pillar wall is thus the result of a combination between a geometrical singularity and multi-body effects.

3 Supplemental figures

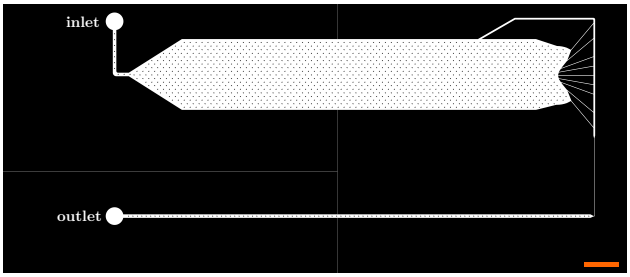

Figure S1: **Geometry of the microfluidic chip 3**.

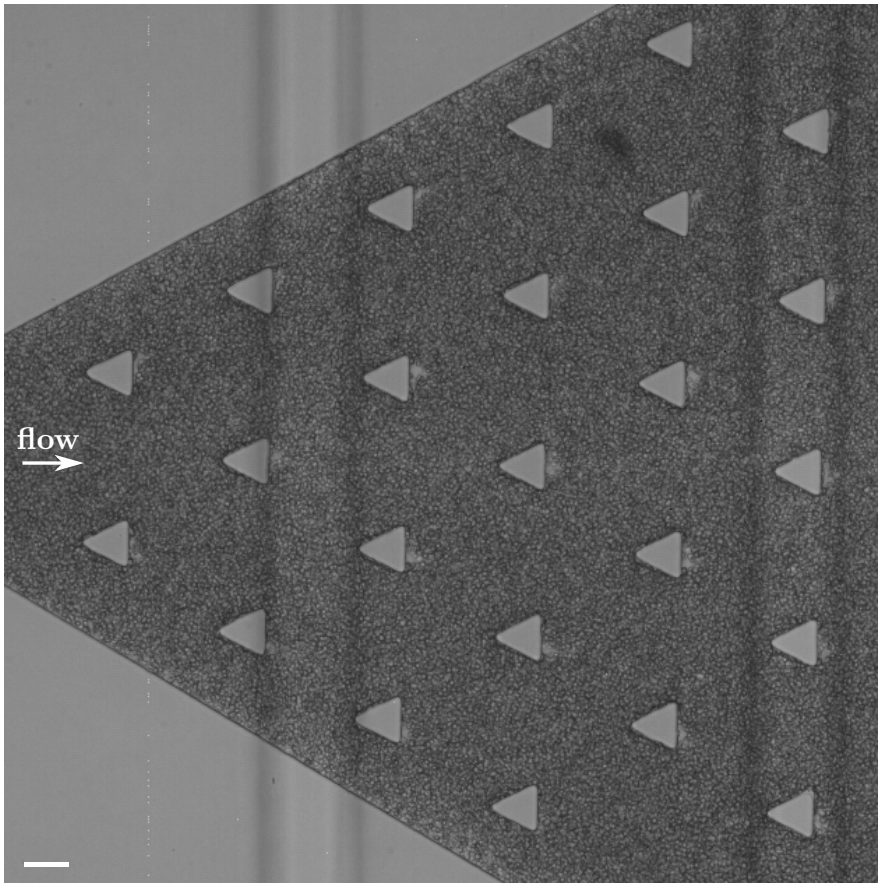

Figure S2: **Absence of aggregation with healthy RBCs.** Picture of the field of view of the microcirculation section of the chip 1 where the triangular posts are present. After 90 minutes of flow, only a few healthy RBCs (sample 11) adhere to the base of the posts. The scale bar is 50 μm.

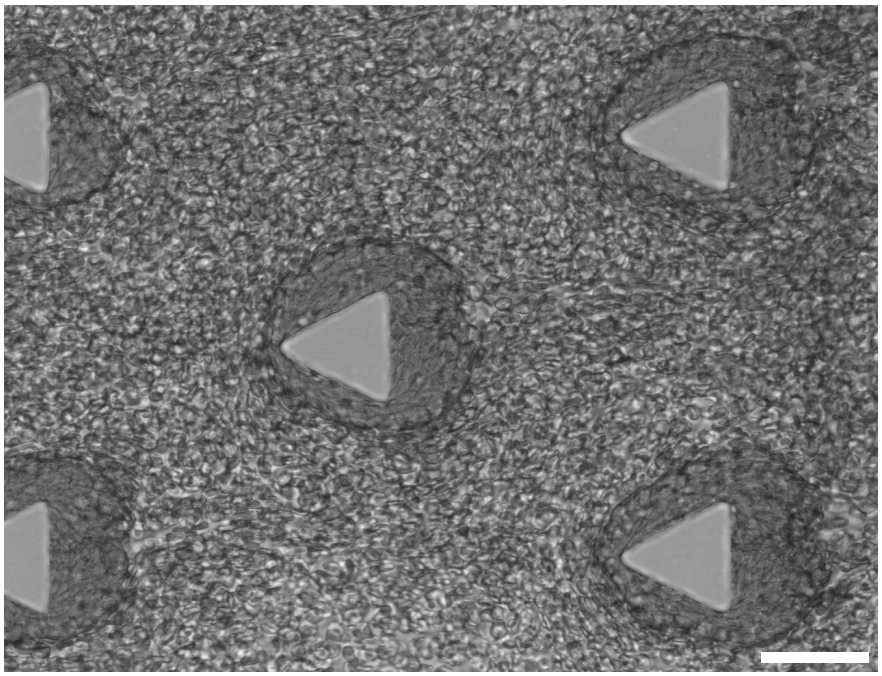

Figure S3: **Aggregate formation under oxygenated conditions.** Picture of the aggregates formed 120 minutes after the initiation of the flow under only oxygenated conditions (sample 4). The scale bar is 50 μm

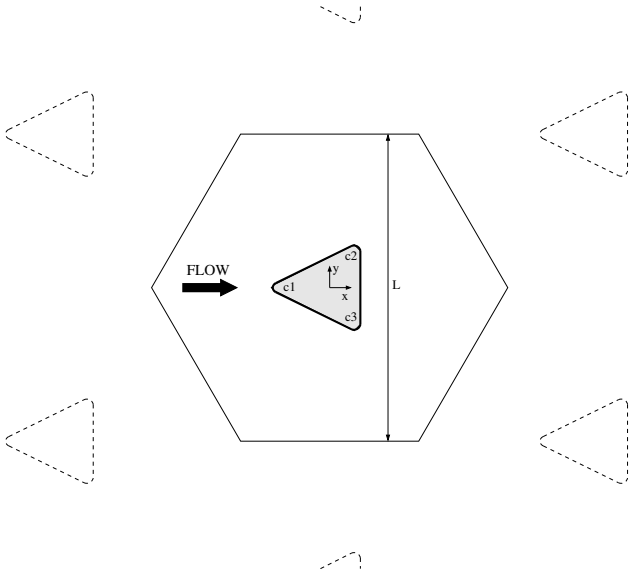

Figure S4: **Schematic of the computational domain (in solid lines) used in the 3-D simulations, over the symmetry plane** $z = 0$. The infinite array of pillars is suggested by the neighboring pillars shotted in dashed lines. In the third direction z (normal to the sheet), the domain is extruded, with wall boundary conditions at $z = \pm 15$ μm.

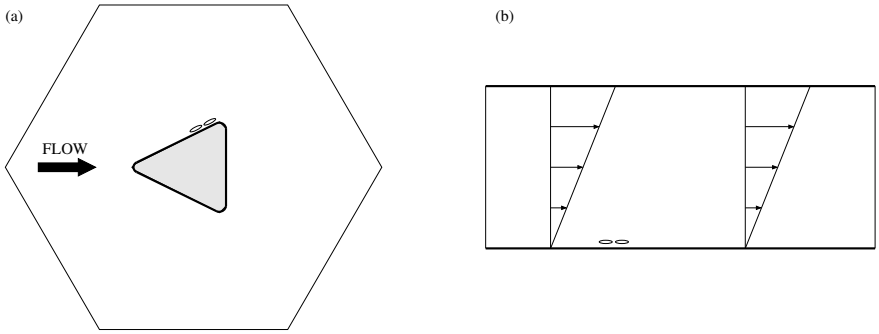

Figure S5: **Two-dimensional configurations used for the dynamics of inextensible capsules near walls**. Thick solid lines are used for solid walls and thin lines for periodic boundary conditions. Two configurations are used: the tri-periodic domain (a) and the Couette flow (b), where the upper wall is moving at prescribed velocity. Small ellipses show the initial locations of the capsules deposited in the flow.

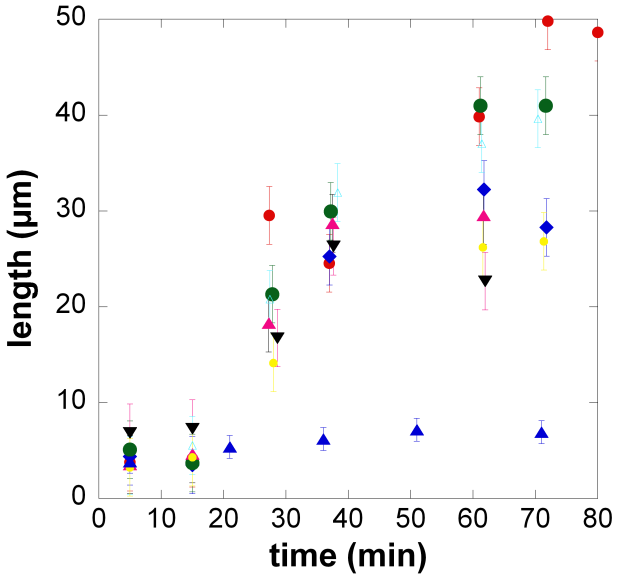

Figure S6: **Temporal evolution of SRBC aggregates at the rear of pillars.** Blood sample from the fraction II, 58% HbS and hematocrit = 25 % in the channels. The blue triangles are for the control experiment with healthy RBCs at the same hematocrit and mean cell hemoglobin concentration.

4 Supplemental movies

movie 1: Timelapse over 1h of aggregation of SRBCs (25% hematocrit, fraction 2, 58% HbS) at the pillar corners, under deoxygenated conditions. The movie start 20 minutes afer the flow has been initiated. First, two aggregates grow at the corners at the rear of a pillar, then after 60 minutes the two aggregates merge together and reach a final size of about 40 μm.
movie 2: Timelapse of SRBCs aggregation under oxygenated conditions. Oxygenated SRBCs are more deformable due to the absence of HbS fibers. This lead to a better alignment of the SRBCs along the the stream flow within the aggregate. Blood sample at 25% hematocrit, fraction II and 58% HbS.
movie 3: Fluctuating aggregate at the rear of a pillar. SRBCs at 25% hematocrit, 58 % HbS and in presence of autologous plasma.
movie 4: detachment of an aggregate from the rear of a pillar. Experimental conditions : SRBCs from the fraction II, 25% hematocrit, 63% HbS.

References

1. Duffy, D., J. McDonald, O. Schueller, and G. Whitesides, 1998. Rapid prototyping of microfluidic systems in poly(dimethylsiloxane). *Anal. Chem.* 70:4974–4984.

2. Vollmer, A., R. Probstein, R. Gilbert, and T. Thorsen, 2005. Development of an integrated microfluidic platform for dynamic oxygen sensing and delivery in a flowing medium. *Lab-on-a-chip* 5:1059–1066.

3. Shiku, H., T. Saito, C. Wu, T. Yasukawa, M. Yokoo, H. Abe, T. Matsue, and H. Yamada, 2006. Oxygen permeability of surface-modified poly(dimethylsiloxane) characterized by scanning electrochemical microscopy. *Chem. Lett.* 35:234–235.

4. Mendez, S., E. Gibaud, and F. Nicoud, 2014. An unstructured solver for simulations of deformable particles in flows at arbitrary Reynolds numbers. *J. Comp. Physics* 256:465–483.

5. Martins Afonso, M., S. Mendez, and F. Nicoud, 2014. On the damped oscillations of an elastic quasi-circular membrane in a two-dimensional incompressible fluid. *J. Fluid Mech.* 746:300–331.

6. Chnafa, C., S. Mendez, and F. Nicoud, 2014. Image-based large-eddy simulation in a realistic left heart. *Comp. Fluids* 94:173–187.

7. Moin, P., and J. Kim, 1982. Numerical investigation of turbulent channel flow. *J. Fluid. Mech.* 118:341–377.

8. Mendez, S., and F. Nicoud, 2008. Large-eddy simulation of a bi-periodic turbulent flow with effusion. *J. Fluid. Mech.* 598:27–65.

9. Moureau, V., P. Domingo, and L. Vervisch, 2011. From Large-Eddy Simulation to Direct Numerical Simulation of a lean premixed swirl flame: Filtered Laminar Flame-PDF modeling. *Comb. and Flame* 158:1340–1357.

10. Malandin, M., N. Maheu, and V. Moureau, 2013. Optimization of the deflated Conjugate Gradient algorithm for the solving of elliptic equations on massively parallel machines. *J. Comp. Physics* 238:32–47.

11. Rusconi, R., S. Lecuyer, N. Autrusson, L. Guglielmini, and H. Stone, 2011. Secondary flow as a mechanism for the formation of biofilm streamers. *Biophys. J.* 100:1392–1399.

12. Peskin, C., 1977. Numerical Analysis of Blood Flow in the Heart. *J. Comp. Physics* 25:220–252.

13. Doddi, S., and P. Bagchi, 2008. Lateral migration of a capsule in a plane Poiseuille flow in a channel. *Int. J. Multiphase Flow* 34:966–986.

14. Ghigliotti, G., T. Biben, and C. Misbah, 2010. Rheology of a dilute two-dimensional suspension of vesicles. *J. Fluid Mech.* 653:489–518.

15. Helfrich, W., 1973. Elastic properties of lipid bilayers: Theory and possible experiments. *Z. Naturforsch.* 28c:693–703.

16. Pozrikidis, C., 2010. Computational Hydrodynamics of Capsules and Biological Cells. *Boca Raton: Chapman & Hall/CRC*.

17. Bagchi, P., 2007. Mesoscale Simulation of Blood Flow in Small Vessels. *Biophys. J.* 92:1858—1877.

18. Ghigliotti, G., H. Selmi, L. El Asmi, and C. Misbah, 2012. Why and how does collective red blood cells motion occur in the blood microcirculation? *Phys. Fluids* 24:101901.

19. Lamura, A., and G. Gompper, 2013. Dynamics and rheology of vesicle suspensions in wall-bounded shear flow. *Europhys. Lett.* 102:28004.

20. Thiébaud, M., Z. Shen, J. Harting and C. Misbah, 2014. Prediction of Anomalous Blood Viscosity in Confined Shear Flow. *Phys. Rev. Lett.* 112:238304.

21. Narsimhan, V., H. Zhao, and E. S. G. Shaqfeh, 2014. Coarse-grained theory to predict the concentration distribution of red blood cells in wall-bounded Couette flow at zero Reynolds number. *Phys. Fluids* 25:061901,1–21.